Article

Inversion and Fine Grading of Tidal Flat Soil Salinity Based on the CIWOABP Model

Jin Zhu [1,†], Shuowen Yang [1,†], Shuyan Li [1], Nan Zhou [1], Yi Shen [2], Jincheng Xing [3,4], Lixin Xu [1], Zhichao Hong [1] and Yifei Yang [1,*]

1   Ocean College, Jiangsu University of Science and Technology, Zhenjiang 212003, China; oscar@just.edu.cn (J.Z.); 221112201125@stu.just.edu.cn (S.Y.); 221112201105@stu.just.edu.cn (S.L.); zhounan@just.edu.cn (N.Z.); Lxu@just.edu.cn (L.X.); hongzhichao@just.edu.cn (Z.H.)
2   The Institute of Industrial Crops, Jiangsu Academy of Agricultural Sciences, Nanjing 210000, China; shenyi@jaas.ac.cn
3   The Salt Soil Agriculture Research Laboratory at Jiangsu Coastal Area Institute of Agricultural Sciences, Yancheng 224000, China; 20101984@jaas.ac.cn
4   Jiangsu Marine Technology Innovation Center, Nantong 226000, China
*   Correspondence: seayyf@just.edu.cn
†   These authors contributed equally to this work.

Abstract: This study on soil salinity inversion in coastal tidal flats based on Sentinel-2 remote sensing imagery is significant for improving saline–alkali soils and advancing tidal flat agriculture. This study proposes an improved approach for soil salinity inversion in coastal tidal flats using Sentinel-2 imagery and a new enhanced chaotic mapping adaptive whale optimization neural network (CIWOABP) algorithm. Novel spectral indices were developed to enhance correlations with salinity, significantly outperforming traditional indexes. The CIWOABP model achieved superior validation accuracy (R^2 = 0.815) and reduced root mean square error (RMSE) and mean absolute error (MAE) compared to other machine learning models. The results enable the precise mapping of salinity levels, aiding salt-tolerant crop cultivation and sustainable agricultural management. This method offers a reliable framework for rapid salinity monitoring and precision farming in coastal regions.

Keywords: tidal flat agriculture; remote sensing inversion; spectral indices; precision breeding

1. Introduction

Soil salinization is one of the main factors restricting sustainable agriculture and ecological environment improvement. According to statistics, approximately 7% of the world's soil is threatened by varying degrees of salinization. Among them, coastal tidal flats are particularly affected by severe salinization [1]. As a special ecological resource in the land–sea interface zone, the coastal tidal flat is an important ecosystem connecting land and sea; it has important economic, social, and environmental values [2]. Consequently, by employing scientific methods and technologies to accurately and reliably monitor changes in soil salinity on tidal flats, this study improves the cultivability of tidal lands and contributes to the management and restoration of saline soils.

Traditional methods for determining soil salinity typically involve pointwise sampling in the field, followed by laboratory analysis of the collected samples. This process is time-consuming, expensive, and can not provide comprehensive data [3]. Optical remote sensing offers several technical advantages, including multiple bands, rich information, and wide coverage. These features enable dynamic, real-time monitoring of soil salinity across large areas, addressing the limitations of traditional methods [4]. Abdalsamad et al. [5]

evaluated the feasibility of using Landsat satellite remote sensing for monitoring surface soil salinity. The study's results demonstrated that this method holds great potential for large-scale soil salinity monitoring and can be effectively used to map the distribution of salt in surface soils. In recent decades, researchers have carried out extensive studies on the spectral characteristics of saline soils [6,7] and remote sensing data sources [8–10]. Considerable progress has also been made in developing methods for soil salinity inversion. Cui et al. [11] employed machine learning algorithms to model and estimate soil salinity at varying depths in farmland under crop cover. The results indicated that the Backpropagation Neural Network (BP) algorithm delivered strong predictive performance, achieving an R-Square (R^2) value of 0.775. This method offers a more cost-effective and spatially extensive approach for monitoring soil salinity in agricultural areas, potentially aiding in soil health management, optimizing irrigation practices, and enhancing crop productivity in salt-affected regions. Additionally, this study highlights the importance of integrating high-resolution remote sensing data with machine learning to achieve accurate and reliable estimates of soil properties at multiple depths. Future work may focus on further refining the models and exploring other remote sensing techniques to improve salinity mapping. Du et al. [12] aimed to address the challenge of timely monitoring of soil water–salt dynamics in croplands. By integrating hybrid spectral unmixing techniques with six machine learning algorithms, this study achieved a significant improvement in the accuracy of soil water–salt dynamic monitoring. Among the models, the eXtreme Gradient Boosting Tree (XGBoost) demonstrated the best performance, achieving an R^2 value of 0.55. This research effectively tackled the difficulties associated with monitoring soil water–salt dynamics in agricultural fields and provided novel methods and insights for estimating soil moisture and salinity in agricultural regions. Sarkar et al. [13] tackled the challenge of soil salinity mapping in the coastal regions of Bangladesh by integrating remote sensing techniques with machine learning algorithms to develop a robust soil salinity inversion model. Among the evaluated models, the Random Forest (RF) model exhibited the highest prediction accuracy. This study not only enhanced mapping precision but also significantly reduced costs and time requirements, offering valuable insights into land resource management and sustainable agricultural practices in coastal areas. Furthermore, this research highlighted the critical role of specific spectral bands, such as shortwave infrared, in salinity prediction, underscoring the efficacy and practicality of combining remote sensing with machine learning methodologies. In conclusion, machine learning algorithms have become widely used in soil salinity inversion research due to their exceptional performance.

Nevertheless, most research has focused on inland salt-affected soils [14–17], while studies on salt-affected soils in coastal tidal flat regions are relatively limited. This is likely due to the complex natural environment of coastal tidal flats, which presents unique challenges for conducting research in these areas. This study integrates remotely sensed data with measured soil salinity data to provide a theoretical foundation for high-precision soil salinity monitoring in tidal flats and precision farming. Building on traditional spectral indices, it selects bands with high correlation to create new spectral indices, thereby enhancing the accuracy of model inversion. The spectral indices with significant correlations were selected and modeled using machine learning algorithms, including the BP, Support Vector Machine (SVM), Random Forest (RF), and the improved BP model CIWOABP. The performance of the models was evaluated using metrics such as R^2, RMSE, and MAE, to identify the optimal model for constructing the soil salinity inversion model. Ultimately, the best-performing model was chosen to conduct soil salinity inversion for the study area, resulting in the creation of a soil salinity map for the region. This study offers significant theoretical and practical contributions to precision farming and breeding in tidal flat agriculture.

2. Materials and Methods

2.1. Study Area

Yancheng is located in the eastern coastal area of China, which owns about 70% of the saline land in Jiangsu Province and a tidal flat area of more than 1.2 million acres [18]. The study area is located at the junction of Dafeng District and Dongtai City in Yancheng City, Jiangsu Province, between $32°57'9''\sim33°2'1''$ N and $120°44'28''\sim120°53'39''$ E, with an east–west length of about 14.359 km, a north–south length of about 11.821 km, and a surface area of about 153.66 km^2 [19]. The tidal flats in the study area are primarily formed through sedimentation and accretion driven by marine dynamics. Soil salinization and alkalization are mainly caused by seawater intrusion and tidal erosion, leading to high soil salinity that significantly impedes vegetation growth and agricultural development [20]. Additionally, the study area is situated in the transitional zone between the subtropical and warm temperate regions. Under the influence of a maritime climate, fluctuating weather conditions lead to an increase in soil pore water salinity, further exacerbating the salinization of the tidal flats [8]. The location map of the study area is presented in Figure 1.
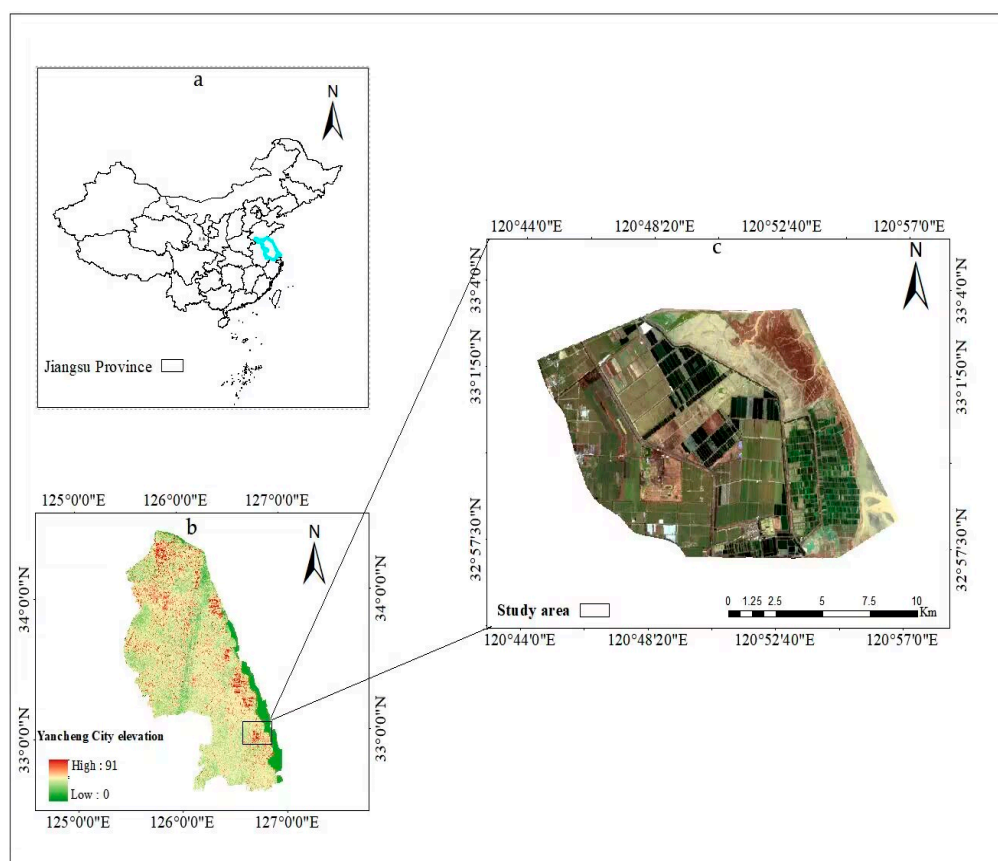

Figure 1. (**a**) The geographical location of Yancheng. (**b**) The elevation model of Yancheng. (**c**) Sampling point area.

2.2. Soil Data Collection and Pretreatment

To ensure the consistency between the ground data collection times and the satellite overpass times, the following plan was implemented: Firstly, a feasible sampling route was designed using map software (https://ditu.amap.com/, accessed on 27 January 2025). Secondly, it was ensured that no sudden changes, such as irrigation or rainfall, occurred during the ground data collection period. Taking into account the soil surface salinity characteristics and land use patterns of the study area, multiple ground soil salinity data collection experiments were conducted in the study area on 14–15 May 2024. During the

sampling period, soil samples were collected using the five-point sampling method, with 21 sampling points selected. Considering that the resolution of the remote sensing data used was 10 m, five sample points were taken within each 10 m^2 area, with a sampling depth ranging from 10 to 20 cm. After drilling the soil samples, they were quickly placed in labeled sampling bags, and the preserved samples were transported to the laboratory for further processing. Simultaneously, the latitude, longitude, and elevation of each sampling point were recorded using a handheld Global Positioning System (GPS) device. The weather during the sampling period was sunny, and no precipitation occurred.

The soil samples collected from the field were brought back to the laboratory for processing. The processing steps primarily included air-drying, grinding, solution preparation, and electrical conductivity measurement [21]. The process for preparing soil samples and measuring their electrical conductivity (EC1:5) is as follows: (1) Place the collected soil samples in a well-ventilated area to air-dry naturally. (2) Once the samples are thoroughly dried, sieve them to remove any impurities, then place the clean soil into ceramic containers. Grind the soil until it becomes a fine powder. (3) Transfer the powdered soil sample into a labeled paper cup, which will be used for solution preparation. (4) When preparing the solution, maintain a soil-to-water mass ratio of 1:5. Mix the soil with water according to this ratio. (5) Use a stirrer to thoroughly mix the solution, ensuring that the soil is fully suspended in the water. (6) Allow the solution to settle for some time, enabling the soil particles to settle at the bottom. (7) After it has settled, filter the solution through filter paper to obtain the supernatant liquid.

The electrical conductivity (EC) measuring instrument was the DDS-307A ($\pm 1.0\%$(FS)) conductivity meter. Finally, the empirical Formula (1) was used to calculate the soil salinity of each sample [22]. The classification criteria for different salinity classes were non-saline soil (<2 g·kg^{-1}), lightly saline soil (2~4 g·kg^{-1}), moderately saline soil (4~6 g·kg^{-1}), heavily saline soil (6~10 g·kg^{-1}), and saline soils (>10 g·kg^{-1}) [23].

$$SSC = (0.282 \times EC_{1:5} + 0.0183) \times 100\% \tag{1}$$

where SSC denotes the soil salt content (g·kg^{-1}); the constant value was determined experimentally and represents the conversion ratio corresponding to the salt content per unit of electrical conductivity.

2.3. Sentinel-2B Satellite Date Preprocessing

The Sentinel system consists of multiple satellites, with Sentinel-2 primarily used for agriculture, land use, and environmental monitoring, particularly for soil, vegetation, and water body monitoring. Its image data across different bands are captured by its multi-spectral imager (MSI), which regularly observes the Earth's surface, capturing data across 13 bands ranging from visible light to shortwave infrared. The experimental data used in this study are Sentinel-2B L1C data, and the downloaded satellite images are synchronized with the soil sampling times in the field. As shown in Table 1, Sentinel-2 images possess multispectral characteristics and high spatial resolution. Initially, Sen2cor, a built-in plug-in of the Sentinel Application Platform (SNAP v7.0) software, was applied for radiometric calibration and atmospheric correction to eliminate the effects of the atmosphere and terrain, resulting in high-quality surface reflectance data. Subsequently, the image data were resampled to 10 m resolution and exported in the TIFF format. The corresponding band combinations were then performed using ENVI5.3. Finally, the band reflectance values at the relevant sampling points were extracted using ArcGIS10.8.

Table 1. Sentinel-2B image parameter.

Band	S2B		Resolution (m)
	Central Wavelength (nm)	**Bandwidth (nm)**	
B1	442.3	45	60
B2 (B)	192.1	98	10
B3 (G)	559.0	46	10
B4 (R)	665.0	39	10
B5	703.8	20	20
B6	739.1	18	20
B7	779.7	28	20
B8 (NIR)	833.0	133	10
B8A	864.0	32	20
B9	943.2	27	60
B10	1376.9	76	60
B11 (SWIR1)	1610.4	141	20
B12 (SWIR2)	2185.7	238	20

2.4. Research on the Salinity Inversion Model

This study uses BP, SVM, RF [24–26], and CIWOABP for simulation tests, and the model with the best accuracy is selected for modeling.

The BP model is a multilayer feedforward network capable of learning and storing the mathematical relationships between a large number of input and output layers. The advantages of the BP model include rapid processing of samples and low computational cost. It can mimic human thought processes to infer and analyze the mechanisms of the model, thereby improving the accuracy and stability of soil salinity inversion models. However, BP also has some drawbacks. The training process of a BP is sensitive to the initial weights. Different initializations of the weights can lead to significant variations in the model's training results. In addition, when training data are insufficient, the BP is prone to overfitting the training data, which impairs the model's ability to generalize to new data. Based on this, this study uses the Whale Optimization Algorithm (WOA) to optimize the BP model [27].

The WOA has advantages such as a simple mechanism, few parameters, and strong optimization capabilities. It simulates humpback whales' unique search strategy and encircling mechanism, which mainly includes three important stages: encircling prey, bubble-net predation, and searching for prey. In WOA, the position of each humpback whale represents a potential solution. By continuously updating the position of the whales in the solution space, the algorithm eventually converges to the global optimal solution [28].

The first stage is the encircling prey phase. The whale's search range covers the entire global solution space, and it is necessary first to determine the position of the prey to surround it. Since the optimal solution's position in the search space is unknown priori, the WOA algorithm assumes that the current best candidate solution is either the target prey or close to the optimal solution. After defining the best search agent, other search agents will attempt to update their positions towards the best search agent. This behavior is implemented by Equations (2)–(5).

$$D = |C \cdot X^*(t) - X(t)| \tag{2}$$

$$X(t + 1) = X^*(t) - A \cdot D \tag{3}$$

$$A = 2a \times r_1 - a \tag{4}$$

$$C = 2 \times r_2 \tag{5}$$

where t represents the current iteration number, A and C are coefficient vectors, X*(t) is the position vector of the current best solution, X(t) is the position vector of the current search agent, a decreases linearly from 2 to 0, and r_1 and r_2 are random vectors in the range [0, 1].

The second stage is the bubble-net predation phase. Humpback whales have two main predation mechanisms: encircling prey and bubble-net predation. In bubble-net predation, the position update between the whale and the prey is expressed by the logarithmic spiral Equations (6) and (7). Since there are two predation behaviors during the approach to the prey, the WOA algorithm chooses either bubble-net predation or shrinking encircling based on a probability *p*. When $p \geq 0.5$, the position update is performed using Equation (6). When $p \leq 0.5$, the position update is performed using Equation (3). As the iteration number t increases, the parameter A and the convergence factor A gradually decrease. When |A| < 1, the whales begin to progressively encircle the current best solution, marking the local search phase in the WOA algorithm.

$$X(t + 1) = D' \times e^{bl} \times \cos(2\Pi l) + X^*(t) \tag{6}$$

$$D' = |X^*(t) - X(t)| \tag{7}$$

where D′ represents the distance between the current search agent and the current best solution, b is the spiral shape parameter, and l is a random number uniformly distributed in the range [−1, 1].

The third stage is the prey search phase. To ensure that all whales thoroughly explore the solution space, WOA updates positions based on the distances between whales, achieving random search. Therefore, when |A| ≥ 1, the search agents move towards a random whale, as described by Equation (9).

$$D'' = |C \cdot X_{rand}(t) - X(t)| \tag{8}$$

$$X(t + 1) = X_{rand}(t) - A \cdot D \tag{9}$$

where D″ represents the distance between the current search agent and a random agent, and $X_{rand}(t)$ denotes the position of the current random agent.

Due to the random initialization of the population in the WOA algorithm, the algorithm's search capability may be insufficient, potentially leading to convergence at local optima. Therefore, this study introduces the Cubic algorithm to optimize the initial population of WOA. The algorithm can escape from local optima by utilizing chaotic mapping for weight search and update. Additionally, an adaptive mechanism is incorporated to optimize the weight coefficient of the shrinking encircling mechanism in WOA, thereby accelerating the model's convergence speed. The cubic formulas are as follows:

$$x_{i+1} = ax_i\left(1 - x_i^2\right) \tag{10}$$

where x_i is the actual value of the spectral index.

The models constructed in this experiment were all regression models, and, therefore, R^2, *RMSE*, and *MAE* were used to comprehensively evaluate the inversion accuracy of the BP, SVM, RF, and CIWOABP models. R^2 reflects the goodness of fit of the regression model, RMSE measures the deviation between the measured and predicted soil salinity values, and MAE represents the absolute error, which provides a better understanding of the actual error in the predicted values. The closer R^2 is to 1 and the smaller the values of *RMSE* and *MAE*, the more accurate the model inversion is. The formulas are as follows:

$$R^2 = 1 - \frac{\sum_{i=1}^{n}\left(y_i - \hat{y_i}^2\right)}{\sum_{i=1}^{n}\left(y_i - \overline{y_i}^2\right)} \tag{11}$$

$$RMSE = \sqrt{\frac{1}{n}\sum_{i=1}^{n}\left(y_i - \hat{y_i}^2\right)} \tag{12}$$

$$MAE = \frac{1}{n}\sum_{i=1}^{n}|y_i - \hat{y_i}| \tag{13}$$

where y_i is the predicted value of soil salt data, $\hat{y_i}$ is the measured value of soil salt data, $\overline{y_i}$ is the mean value of the original soil salt data, and n is the number of samples.

The technical flowchart of this study is shown in Figure 2. Soil samples were first collected from the study area, and the longitude and latitude information of each sampling point was recorded in this study. The soil samples were then sent to the laboratory to obtain the salinity data for each sampling point. Subsequently, the salinity data were divided into the modeling and validation datasets. The Sentinel-2B imagery was then preprocessed, and the reflectance values of the image bands at the sampling points were extracted using the latitude and longitude information. Next, a correlation analysis was performed between the band reflectance values and the measured soil salinity data. Based on traditional spectral indices, bands with high correlation were selected to create new spectral indices to improve the accuracy of the model's inversion. The optimal spectral index was then chosen as the model's input, and the salinity data from the modeling dataset were used as the output to train the machine learning model. The model was validated using the validation dataset to assess its accuracy and identify the best-performing model. Finally, the selected optimal model was used for soil salinity inversion in the study area, generating a salinity map for the region.
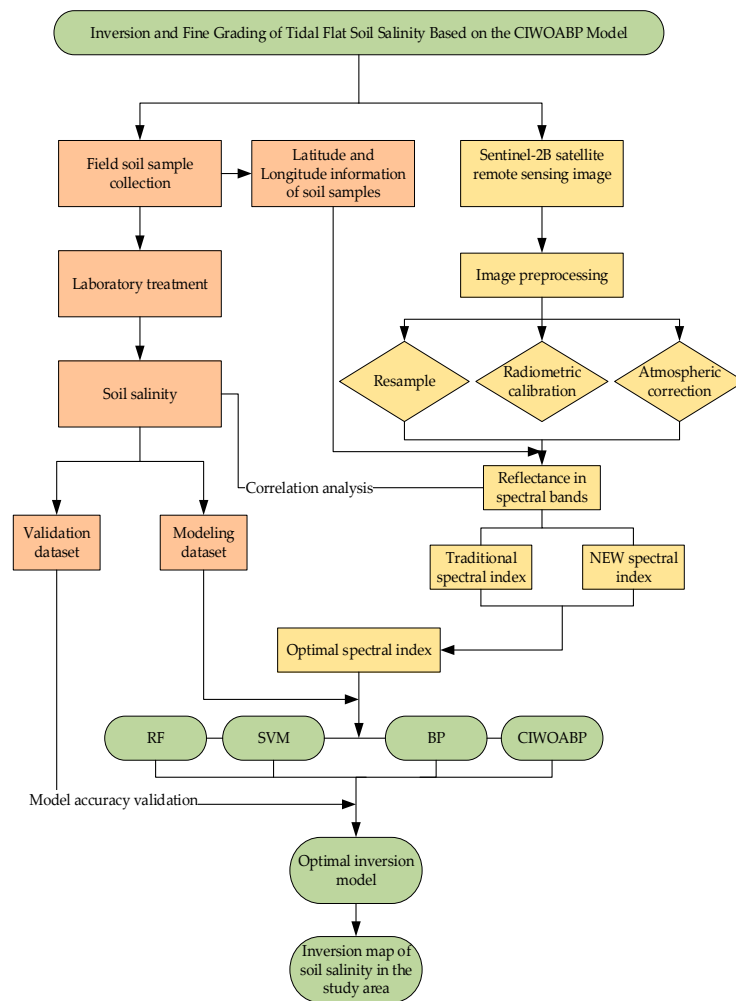

Figure 2. Technology flowchart of this study.

3. Results and Analysis

3.1. The Correlation Between Multispectral Reflectance and Measured Soil Salt Content

After preprocessing, the reflectance of commonly used Sentinel-2 image bands (Blue(B), Green(G), Red(R), NIR, SWIR1, SWIR2) was analyzed for Pearson correlation with soil salinity. The results are shown in Table 2. Among the individual bands, the correlation between reflectance and soil salinity in the NIR band was found to be insignificant, while the reflectance of the B, G, R, SWIR1, and SWIR2 bands showed a significant positive correlation with soil salinity. Among these, the SWIR1 band exhibited the strongest correlation, with a correlation coefficient of 0.511.

Table 2. The correlation coefficient between each band's reflectance and salt content.

Band	B	G	R	NIR	SWIR1	SWIR2
Correlation coefficient	0.369 *	0.408 *	0.437 *	0.174	0.511 **	0.396 *

*: significant at $p < 0.05$ level; **: significant at $p < 0.01$ level.

Spectral indices are derived using remote sensing technology by combining various visible and infrared bands from satellite multispectral imagery to enhance specific spectral characteristics. These indices are used to highlight specific features of ground objects. Among them, the Salinity Index (SI) is a crucial metric for quantitatively assessing surface salinity conditions. This study selected 11 commonly used traditional salt indices [29–36] for quantitative analysis of soil salt content. As shown in Table 3, among the spectral indices derived from multiple bands, SI, SI1, SI2, SI3, and S3 exhibited significant correlations with the measured soil salt content, with correlation coefficients of 0.42, 0.43, 0.37, 0.43, and 0.43, respectively. The correlation between the other spectral indices and the measured soil salt content was found to be weak.

Table 3. Spectral index formula and its correlation with salinity.

	Formulation	Correlation Coefficient
SI-T	$R/NIR \times 100$	0.30
SI	$(B \times R)^{1/2}$	0.42 *
SI1	$(G \times R)^{1/2}$	0.43 *
SI2	$(G^2 + R^2 + NIR^2)^{1/2}$	0.37 *
SI3	$(G^2 + R^2)^{1/2}$	0.43 *
S1	B/R	−0.11
S2	$(B - R)/(B + R)$	−0.11
S3	$G \times R/B$	0.43 *
ESI	$((B \times R)^{1/2} + SWIR1)/SWIR1$	0.11
ES2	$(B - R + SWIR2)/(B + R + SWIR2)$	0.25
ENDSI	$(R - NIR)/(R + NIR + SWIR2)$	0.28

*: significant at $p < 0.05$ level.

The correlation of traditional spectral indices is generally low, typically below 0.50. Developing spectral indices with a high correlation is crucial to enhance the model's accuracy, specifically tailored to the salinity characteristics of the tidal flats. The basic principle of creating spectral indices is identifying the bands with the strongest and weakest reflections for the target land cover within multispectral bands. Through geometric operations, the difference between these two bands is further amplified in a geometric progression [37]. This process enhances the brightness of the target land cover in the resulting index image while suppressing the background land cover. Therefore, this study replaced the low-correlation bands in SI, SI1, SI2, SI3, and S3 with the high-correlation SWIR1 band, and

constructed new spectral indices (NEWSI4, NEWSI5, NEWSI6, NEWSI7, and NEWSI8). This modification enhanced the representativeness of the spectral indices in reflecting the salinity characteristics of the study area. As shown in Table 4, the new spectral indices, after incorporating SWIR1, exhibited significantly stronger correlations with soil salinity. The correlation coefficients were all approximately 0.5, generally higher than those of the traditional spectral indices presented in Table 3, with the highest correlation of 0.52 observed for NEWSI6.

Table 4. New spectral index formula and its correlation with salinity.

Spectral Index	Formulation	Correlation Coefficient
NewSI4	$(G \times SWIR1)^{1/2}$	0.51 *
NewSI5	$(R \times SWIR1)^{1/2}$	0.50 *
NewSI6	$(G^2 + R^2 + SWIR1^2)^{1/2}$	0.52 *
NewSI7	$(R^2 + R^2 + SWIR1^2)^{1/2}$	0.52 *
NewSI8	$(R^2 + SWIR1^2)^{1/2}$	0.52 *

*: significant at $p < 0.05$ level.

To reduce redundant information and improve the model's interpretability, this study performed collinearity analysis on the aforementioned spectral indices. As shown in Figure 3, there is a high degree of collinearity between different spectral indices. These redundant data could increase the complexity of model training and even lead to overfitting issues [35]. Therefore, it is necessary to select spectral indices with higher correlation to avoid noise interference and enhance the model's predictive ability. Ultimately, to enhance the model's generalization capability, this study selected the spectral indices SWIR1 and NEWSI6, which showed significant correlation, as input variables for the regression model. These were used to establish the quantitative relationship between remote sensing images and soil salinity.
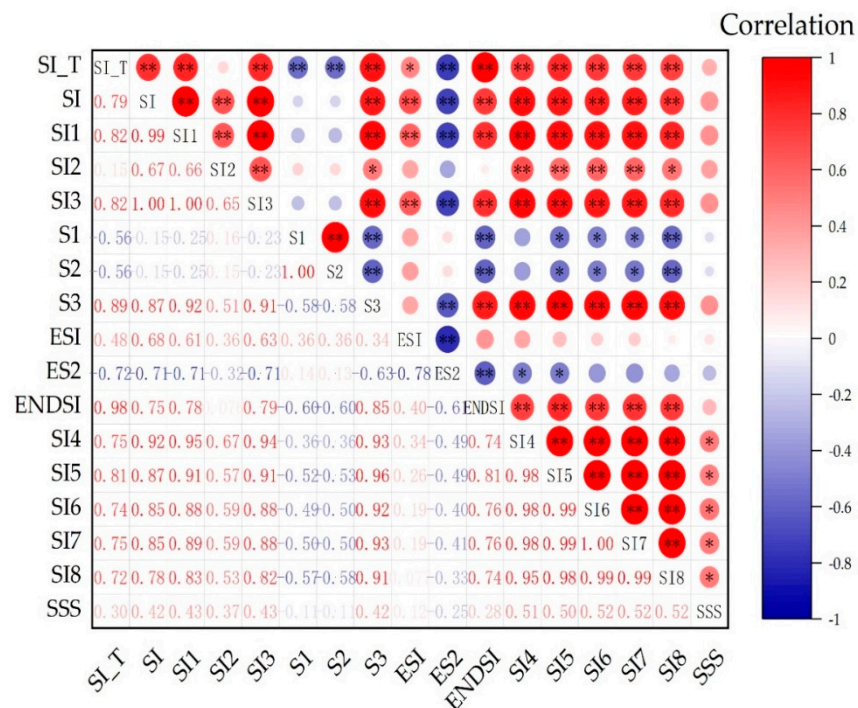
Figure 3. Correlation heatmap analysis of spectral indices.

3.2. Soil Salinity Prediction Model

In this study, 21 soil samples were collected, with their salt content arranged in ascending order. The samples were then selected using an interval sampling method, where 14 samples were designated for model training and the remaining 7 samples were set aside for model accuracy testing. The spectral indices SWIR1 and NEWSI6 were used as independent variables, and the measured salt data were used as dependent variables. Four machine learning models, BP, SVM, RF, and CIWOABP, were used to create soil salt inversion models.

As shown in Table 5, when the SWIR1 band is used for modeling, the CIWOABP model demonstrates the best fit. The R^2 values for the training and validation sets are 0.712 and 0.763, respectively, surpassing those of the RF, SVM, and BP models. Furthermore, the model performs better on the validation set than on the training set, suggesting a strong generalization ability. The results from the training set indicate that the BP model outperforms the SVM model in all parameters. This is likely due to its strong nonlinear mapping capability, as its multi-layer structure allows for the abstraction of the data, enabling it to learn hierarchical features and model complex data more effectively. Although SVM can also handle nonlinear data, its nonlinear ability is limited by the choice of kernel function and parameter settings, which can affect the training results. However, the overall performance of the BP model is slightly lower than that of the RF model. This may be because the RF model, consisting of multiple decision trees, reduces the risk of overfitting through ensemble learning, allowing it to fit data better in most cases, especially with small datasets. Compared to the other three models, the CIWOABP model achieved the highest R^2 value of 0.712. When compared to the SVM model, the CIWOABP model reduced the RMSE and MAE values by 0.507 g·kg^{-1} and 0.164 g·kg^{-1}, respectively. This improvement can be attributed to the integration of chaotic mapping and the adaptive whale optimization algorithm in the CIWOABP model, which enhances its global search capabilities and optimizes the network weights. As a result, the model is better equipped to identify more appropriate mapping relationships within complex nonlinear data, leading to improved prediction accuracy. In the validation set, the CIWOABP model achieved an RMSE value of 0.601 g·kg^{-1}, the lowest among all four models, and the MAE value was reduced by 0.229 g·kg^{-1} compared to the RF model and by 0.087 g·kg^{-1} compared to the BP model. As shown in Figure 4, the RF, SVM, and BP models performed better in predicting low-salinity samples. In contrast, the prediction accuracy for low-salinity samples was generally higher than for high-salinity samples. The CIWOABP model demonstrated good prediction performance for both low and high-salinity samples. Although some predictions showed minor deviations, the overall predicted values were proportional to the actual measured values, indicating a good fit and enhanced model stability.

Table 5. Soil salinity inversion results from different models.

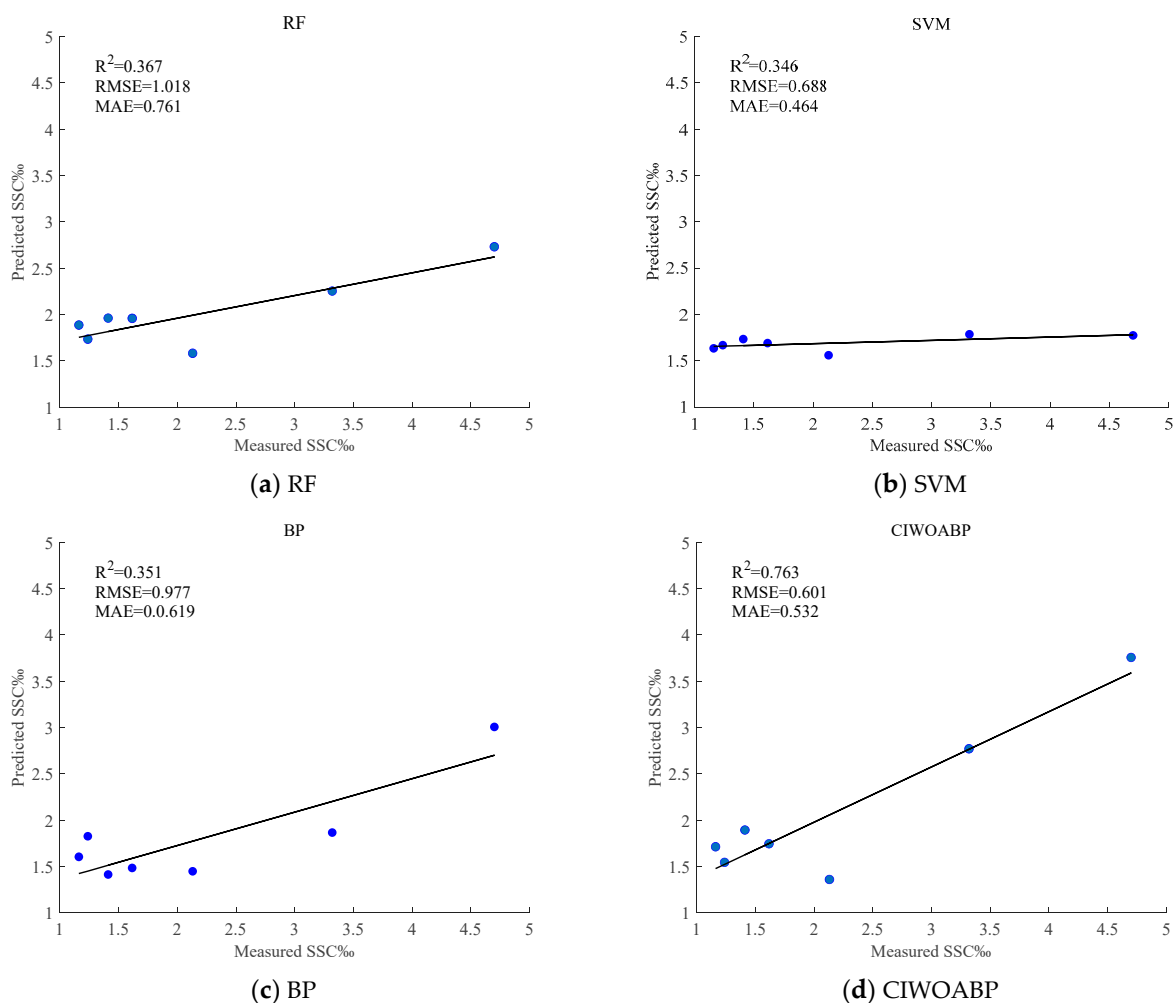| Model	B11						B11 + NEWSI6					
	Train			Test			Train			Test		
	R^2	RMSE	MAE	R^2	RMSE	MAE	R^2	RMSE	MAE	R^2	RMSE	MAE
RF	0.503	0.683	0.458	0.367	1.018	0.761	0.611	0.579	0.434	0.332	1.10	0.850
SVM	0.251	1.342	0.751	0.346	0.688	0.464	0.352	0.906	0.549	0.313	0.620	0.719
BP	0.308	0.834	0.550	0.351	0.977	0.619	0.666	0.665	0.522	0.658	0.437	0.349
CIWOABP	**0.712**	**0.835**	**0.587**	**0.763**	**0.601**	**0.532**	**0.874**	**0.332**	**0.223**	**0.815**	**0.531**	**0.454**

Figure 4. Soil salinity prediction figure based on spectral index B11, with blue dots representing predicted values.

Additionally, as shown in Table 5, the introduction of the new spectral index NEWSI6 resulted in an improvement in the R^2 values for the RF, SVM, BP, and CIWOABP models, while the RMSE values in the training set were all reduced, indicating better model fit. Among the models, the CIWOABP model exhibited the best overall performance. The R^2 values for the training and validation sets were the highest among the four models, reaching 0.874 and 0.815, respectively. These values represent an increase of 0.162 and 0.052 compared to the model using only the SWIR1 spectral index. Additionally, both RMSE and MAE values were reduced, demonstrating that the new spectral index introduced in this study significantly enhances the inversion accuracy of the models. Furthermore, the CIWOABP model exhibits the lowest RMSE and MAE values in the training set compared to the RF, SVM, and BP models. On the validation set, the RMSE and MAE values of the CIWOABP model are also lower than those of the RF and SVM models. As shown in Figure 5, RF and SVM demonstrate slight improvements in predicting low-salinity samples but show limited progress in predicting high-salinity samples. In contrast, the BP model improves performance in predicting high salinity samples, indicating its better handling of these cases. The CIWOABP model shows a good fit to the 1:1 line for both low and high-salinity samples, with predictions for low-salinity samples scattered around the 1:1 line and high-salinity samples aligning closely with it. This demonstrates the model's strong generalization ability and superior predictive performance. As observed in Figures 4

and 5, the CIWOABP model is robust and stable, consistently providing reliable results across different salinity levels.
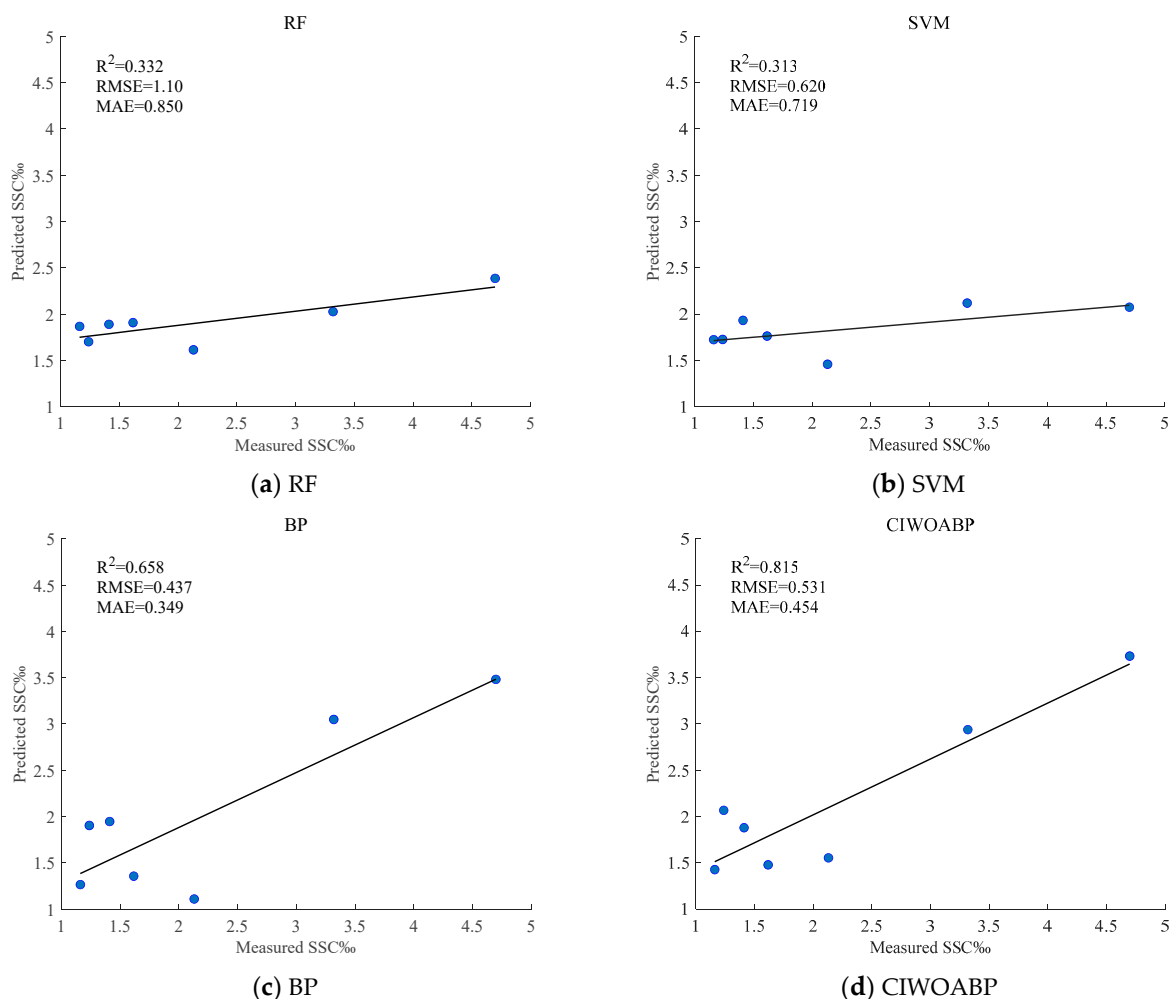

Figure 5. Soil salinity prediction figure based on spectral index B11 and SI6, with blue dots representing predicted values.

In conclusion, the CIWOABP model proposed in this study demonstrates a strong generalization capability. It not only achieves high accuracy on the training dataset but also maintains excellent predictive performance on the test dataset. The model's robustness allows it to resist the influence of noise and outliers, making it suitable for practical applications. Moreover, the model does not exhibit significant overfitting, and its generalization error remains low, indicating that it has a strong generalization ability and can be reliably applied for soil salinity inversion in the study area.

3.3. Soil Salinity Inversion

According to the soil salinity classification standard, the study area covered by the sampling points was divided into five salinity types: non-saline, mildly saline, moderately saline, heavily saline, and saline soils. The soil salinity inversion results for the study area are shown in Figure 6. The salinization levels from low to high are as follows: 31.63%, 42.47%, 12.77%, 7.62%, and 5.51%.
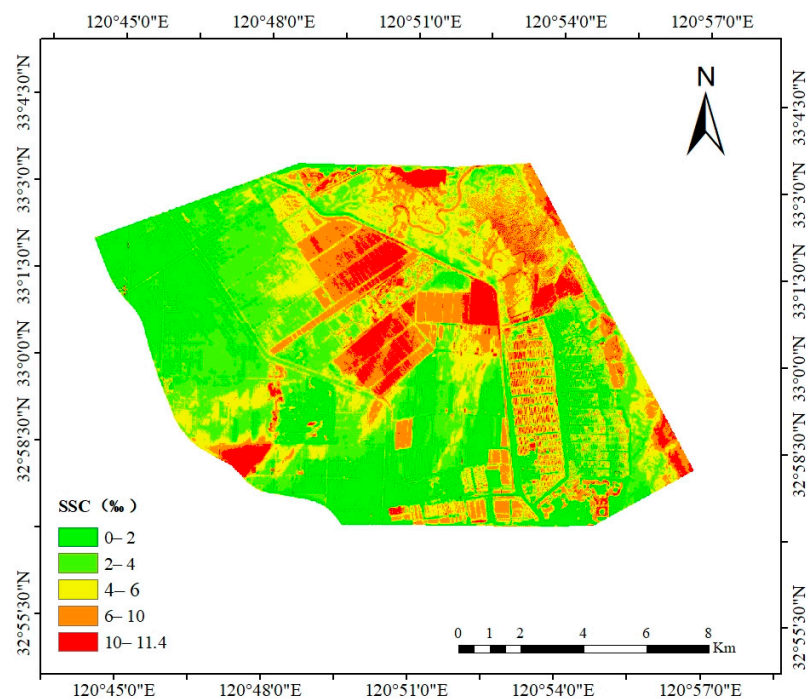
Figure 6. The salinity inversion map of the study area, where darker colors indicate higher soil salinity levels.

As shown in Figure 6, the salinity map of the study area generally exhibits a west-to-east gradient, with lower salinity in the west and higher salinity in the east. There is a clear east–west differentiation along the coastal highway. The eastern coastal areas have higher salinity levels and are dominated by saline soils, which is consistent with the field survey results. Except for the fish ponds, the western region mainly consists of non-saline and mildly saline soils suitable for crop cultivation, accounting for 74.1% of the total. The significant east–west salinity difference in the study area is primarily due to the eastern region's proximity to the seawater, relatively low elevation, and shallow groundwater table, which is influenced by seawater intrusion, leading to increased groundwater salinity. Additionally, the region's high temperatures and intense evaporation rates further exacerbate the soil salinization process. In the western part of the study area, the coastal highway acts as a natural barrier, leading to relatively lower salinity levels. However, in the southwestern region, which lies within a groundwater funnel zone, extensive groundwater extraction and large-scale irrigation for agriculture have facilitated the infiltration of mineralized groundwater into the soil. This has resulted in the development of moderately to severely saline soils in certain areas.

3.4. Fine Classification of Farmland in the Study Area Combined with Local Crops

The saline–alkali tidal flats represent a significant strategic reserve for improving the quality, increasing efficiency, and expanding the capacity of China's arable land, serving as a potential "granary" for the nation's grain production. This study classified remote sensing image data of the research area using a Support Vector Machine (SVM) in ENVI5.3. The classification achieved an accuracy of 98.45%, with a kappa coefficient of 0.98, indicating excellent classification performance. The vector file exported from the classification is shown in Figure 7. The extracted data were then segmented in ArcGIS10.8 to identify the farmland areas, which were combined with local crop information. This approach provides a theoretical reference for salinity management in the precision breeding of local salt-tolerant crops.
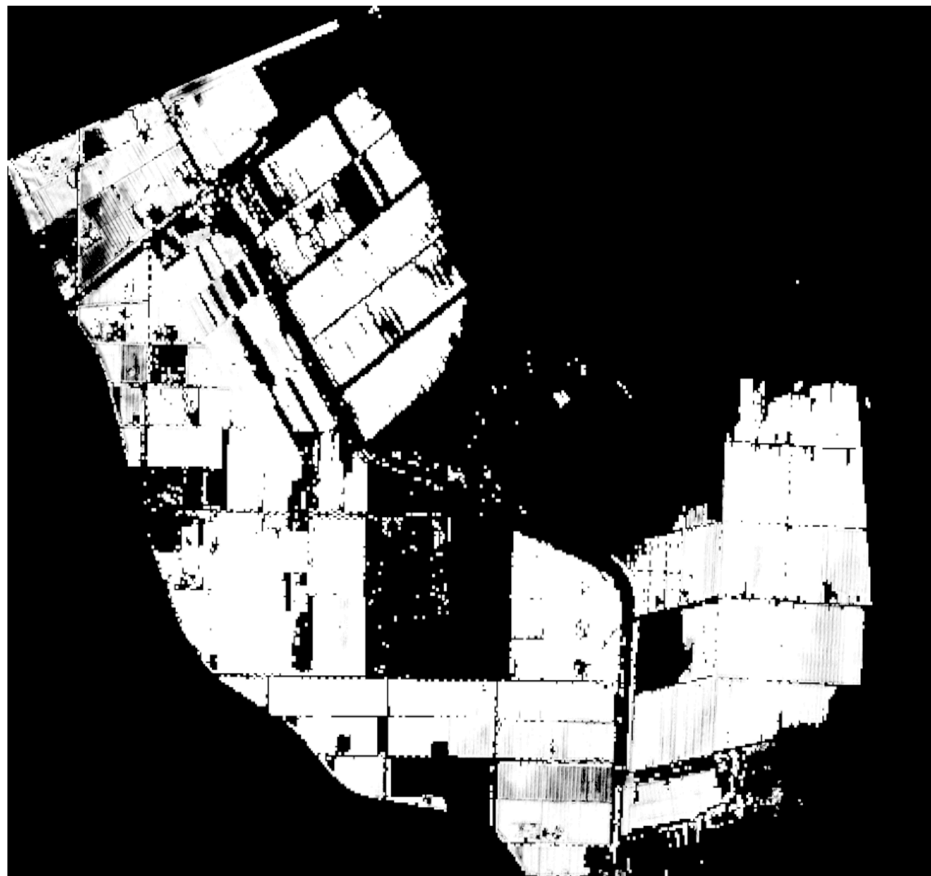
Figure 7. The vector file of farmland in the study area, where white represents farmland.

Based on the seasonal requirements of the crops, three common local salt-tolerant crops were selected: salt-tolerant maize, salt-tolerant rice, and Seepweed. The distribution of these crops is shown in Figure 8. Salt-tolerant maize, which resists lodging and has a high yield and market value, is generally less tolerant to salt stress. Therefore, salt-tolerant maize is recommended for planting on land with salinity levels below 2‰ in the study area, as indicated by the blue area in Figure 8. Additionally, one-third of the arable land in Dongtai City lies within the Lishai River water network area, a natural and healthy base for rice production, with 98,860 acres of rice planted year-round, ranking among the top in Jiangsu province. Some salt-tolerant rice varieties can tolerate salinity levels between 2‰ and 6‰, as shown in the yellow area in Figure 8. These rice varieties can be selected for planting to increase the economic benefits of saline agricultural land. The local specialty crop Seepweed can be planted for heavily saline and saline soils. Seepweed is highly salt-tolerant and selectively absorbs soluble salt ions, improving the fertility of saline soils. Furthermore, it is rich in nutrients and serves as a high-quality vegetable and oilseed crop. The inner stems and leaves of Seepweed can be consumed both fresh and dried, making it easy to store and transport. The development of Seepweed as a vegetable crop shows great potential. As indicated by the red area in Figure 8, planting Seepweed can enhance the efficiency of saline soil utilization and management.
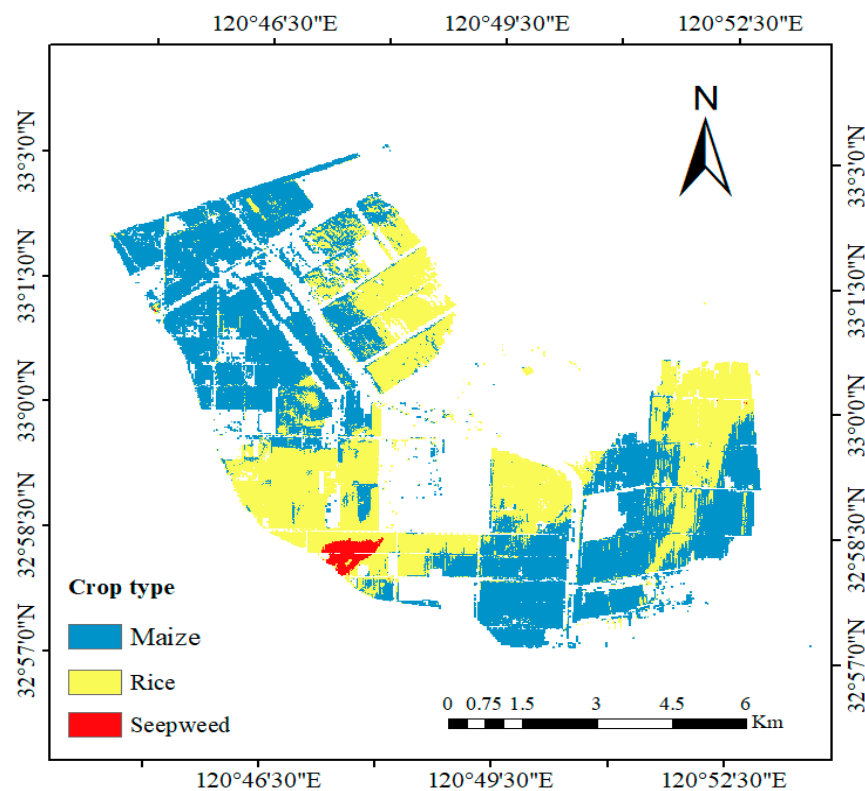
Figure 8. The precision breeding map of the study area, where light blue represents maize, yellow represents rice, and red represents seepweed.

4. Discussion

Previous studies on soil salinity inversion have predominantly focused on inland farmland or saline–alkali land, where traditional salt indices or vegetation indices were used for modeling [38]. However, tidal flats, formed through sedimentation and siltation driven by marine dynamics, present a much more complex environmental context. The soil texture of tidal flat farmland differs significantly from that of inland areas [2]. This study finds that the correlation between traditional spectral indices and soil salinity is generally low (as shown in Table 3), which can be attributed to the complex soil texture of coastal and tidal flat farmlands. As a result, traditional spectral indices may not be suitable for salt inversion in this context. To overcome this limitation, a new spectral index has been proposed to improve the accuracy of the models. As shown in Tables 4 and 5, the new spectral index outperforms models constructed solely with the B11 band, leading to enhanced prediction accuracy across all models. This finding underscores the significant impact that the selection of input variables can have on the model's performance in predicting soil salt content. Consequently, it is crucial to selectively choose spectral indices tailored to the research environment's specific characteristics to enhance model accuracy. Moreover, the salinization of tidal flat soils is influenced by a variety of factors, including elevation, precipitation, temperature, soil texture, groundwater level, and vegetation cover [39]. Future studies on mudflat soil salinization should consider these factors comprehensively to better understand the process and develop effective management strategies.

Machine learning algorithms offer robust data-mining capabilities and exceptional non-linear fitting abilities, making them highly effective for modeling the complex, non-linear relationships between soil salinity and its influencing factors. Selecting an appropriate modeling approach is, therefore, critical for improving the accuracy and reliability of predictions [40]. In this study, it was observed that the CIWOABP model more effectively captures the complex, non-linear relationship between spectral indices and soil salinity. This

improvement is primarily attributed to the adaptive mechanism integrated into the model, which enhances its ability to adapt to varying data. Moreover, as shown in Figures 4 and 5, the CIWOABP model demonstrated greater stability compared to the other three models throughout both experimental prediction processes. This enhanced stability is a result of the integration of chaotic mapping algorithms and whale optimization algorithms, which improve the model's optimization capabilities. As a result, the CIWOABP model exhibits superior generalization ability and robustness during the fitting process. Furthermore, the experiments revealed that all four models tended to underestimate high-salinity data while overestimating low-salinity data. This phenomenon may be attributed to the significant spatial variability of soil salinity, where the pixel values in the remote sensing images reflect averaged spectral characteristics over a given coverage area. As a result, the inversion of individual pixel salinity experiences a smoothing effect, leading to inaccuracies in the prediction of both high- and low-salinity areas [41]. In addition, studies have shown that soil texture, the environment of sampling points, and the depth of sampling points can significantly influence the soil salinity at these points, thereby affecting the model's fitting accuracy [42–44].

In terms of soil salinity, the salt inversion results obtained in this study can provide valuable theoretical guidance for crop cultivation in the research area. In selecting salt-tolerant crop varieties, we consulted with local agricultural researchers and conducted field surveys, as shown in Figure 8, ultimately choosing three commonly grown salt-tolerant crops in the region. When planning crop cultivation, it is essential to consider the characteristics of these crops further to optimize planting decisions. In addition to economic benefits, it is also crucial to ensure that the selected crops can, to some extent, improve the soil structure of saline–alkali lands and enhance soil fertility.

5. Conclusions

Most scholars have conducted limited research on tidal flats due to their complex natural environment, overlooking their significant research value. This study uses Sentinel-2B multispectral remote sensing imagery as the data source, develops a new spectral index for saline soils, and combines it with the improved CIWOABP model to perform salinity inversion in the study area. Based on this, this study conducts precise breeding analysis for the entire farmland in the region from the salinity perspective, incorporating local crop information.

Compared to conventional spectral indices, the new spectral index proposed in this study significantly enhances the correlation between the spectral indices and measured soil salinity, thereby improving the accuracy of soil salinity inversion. The improved CIWOABP model outperforms the other three simpler machine learning models, demonstrating a stronger linear relationship between the model's predicted values and the measured values; after the inclusion of the new spectral index, the R^2 value of the validation set reached 0.815, indicating that this model is both stable and accurate, with successful results in soil salinity inversion for the study area. The inversion results reveal a clear east–west differentiation in soil salinity within the study area. Generally, the western region exhibits low salinity, dominated by non-saline and slightly saline soils, while the eastern coastal areas have higher salinity levels, primarily consisting of saline soils. This pattern is consistent with field survey observations. Most of the agricultural land in the study area has salinity levels below 6‰, making it suitable for planting salt-tolerant crops such as corn and rice. In areas with higher salinity due to groundwater extraction and irrigation, salt-tolerant crops like Seepweed can be cultivated to improve soil fertility and enhance economic benefits.

Although this study has yielded good results, there are still some limitations. For example, the spatial resolution of Sentinel-2B may not fully capture the subtle variations in

salinity. Additionally, environmental factors such as climate, precipitation, and terrain have a significant impact on soil salinity, which may affect the generalizability and applicability of the results. Future research should pay more attention to the influence of these factors. In conclusion, in the context of limited land and labor resources, the effective utilization of tidal flat saline–alkali land represents a valuable land resource that can support agricultural development and contribute to ecological conservation, aligning with the goals of sustainable development. If not properly managed, however, these areas may become severely degraded, leading to ecological deterioration. Therefore, research into precision breeding and the comprehensive utilization of saline–alkali land is strategically crucial for ensuring national food security and safeguarding China's agricultural future.

Author Contributions: J.Z.: Conceptualization, methodology, software, validation, and writing—original draft preparation; S.Y.: formal analysis, investigation, visualization, resources, writing—original draft preparation, and writing—review and editing; S.L.: resources and data curation; N.Z.: writing—review and editing; Y.S.: supervision; J.X.: project administration; L.X.: funding acquisition; Z.H.: resources; Y.Y.: resources; All authors have read and agreed to the published version of the manuscript.

Institutional Review Board Statement: Not applicable.

Data Availability Statement: The data presented in this study are available upon request from the corresponding author. The data are not publicly available due to confidentiality concerns.

Conflicts of Interest: The authors declare no conflicts of interest.

References

1. Alexakis, D.; Daliakopoulos, I.N.; Panagea, I.S.; Tsanis, I.K. Assessing soil salinity using WorldView-2 multispectral images in Timpaki, Crete, Greece. *Geocarto Int.* **2018**, *33*, 321–338. [CrossRef]
2. Guo, J.; Ma, Y.; Ding, C.; Zhao, H.; Cheng, Z.; Yan, G.; You, Z. Impacts of Tidal Oscillations on Coastal Groundwater System in Reclaimed Land. *J. Mar. Sci. Eng.* **2023**, *11*, 2019. [CrossRef]
3. Wang, J.; Sun, Q.; Shang, J.; Wu, F.; Dai, Q. A new approach for estimating soil salinity using a low-cost soil sensor in situ: A case study in saline regions of China's East Coast. *Remote Sens.* **2020**, *12*, 239. [CrossRef]
4. Peng, J.; Biswas, A.; Jiang, Q.; Zhao, R.; Hu, J.; Hu, B.; Shi, Z. Estimating soil salinity from remote sensing and terrain data in southern Xinjiang Province, China. *Geoderma* **2019**, *337*, 1309–1319. [CrossRef]
5. Aldabaa, A.A.A.; Weindorf, D.C.; Chakraborty, S.; Sharma, A.; Li, B. Combination of proximal and remote sensing methods for rapid soil salinity quantification. *Geoderma* **2015**, *239*, 34–46. [CrossRef]
6. Mohamed, S.A.; Metwaly, M.M.; Metwalli, M.R.; AbdelRahman, M.A.E.; Badreldin, N. Integrating Active and Passive Remote Sensing Data for Mapping Soil Salinity Using Machine Learning and Feature Selection Approaches in Arid Regions. *Remote Sens.* **2023**, *15*, 1751. [CrossRef]
7. Wang, L.; Hu, P.; Zheng, H.; Liu, Y.; Cao, X.; Hellwich, O.; Chen, X. Integrative modeling of heterogeneous soil salinity using sparse ground samples and remote sensing images. *Geoderma* **2023**, *430*, 116321. [CrossRef]
8. Jia, P.; He, W.; Hu, Y.; Liang, Y.; Liang, Y.; Xue, L. Inversion of coastal cultivated soil salt content based on multi-source spectra and environmental variables. *Soil Tillage Res.* **2024**, *241*, 106124. [CrossRef]
9. Kholdorov, S.; Lakshmi, G.; Jabbarov, Z.; Yamaguchi, T.; Yamashita, M.; Samatov, N.; Katsura, K. Analysis of Irrigated Salt-Affected Soils in the Central Fergana Valley, Uzbekistan, Using Landsat 8 and Sentinel-2 Satellite Images, Laboratory Studies, and Spectral Index-Based Approaches. *Eurasian Soil Sci.* **2023**, *56*, 1178–1189. [CrossRef]
10. Cui, X.; Han, W.; Zhang, H.; Cui, J.; Ma, W.; Zhang, L.; Li, G. Estimating soil salinity under sunflower cover in the Hetao Irrigation District based on unmanned aerial vehicle remote sensing. *Land Degrad. Dev.* **2023**, *34*, 84–97. [CrossRef]
11. Cui, J.; Chen, X.; Han, W.; Cui, X.; Ma, W.; Li, G. Estimation of soil salt content at different depths using UAV multi-spectral remote sensing combined with machine learning algorithms. *Remote Sens.* **2023**, *15*, 5254. [CrossRef]
12. Du, R.; Chen, J.; Lang, Y.; Lang, R.; Yang, X.; Wang, T.; Chen, Y. Timely monitoring of soil water-salt dynamics within cropland by hybrid spectral unmixing and machine learning models. *Int. Soil Water Conserv. Res.* **2024**, *12*, 726–740. [CrossRef]

13. Sarkar, S.K.; Rudra, R.R.; Sohan, A.R.; Das, P.C.; Ekram, K.M.M.; Talukdar, S.; Islam, A.R.M.T. Coupling of machine learning and remote sensing for soil salinity mapping in coastal area of Bangladesh. *Sci. Rep.* **2023**, *13*, 17056. [CrossRef]

14. Salcedo, F.P.; Cutillas, P.P.; Cabañero, J.J.A.; Vivaldi, A.G. Use of remote sensing to evaluate the effects of environmental factors on soil salinity in a semi-arid area. *Sci. Total Environ.* **2022**, *808*, 152524. [CrossRef] [PubMed]

15. Dusingizimana, M.W.; Friedrich, A.M.; Kahle, B.; Rieger, S.M.; Heuss-Aßbichler, S.; Závada, P.; Zebari, M. Using ASTER Multispectral and EnMAP Hyperspectral Remote Sensing for Lithological Map of Salt Diapirs in the Zagros Mountains, Iran. In Proceedings of the EGU General Assembly 2024, Vienna, Austria, 14–19 April 2024.

16. Li, Y.; Chang, C.; Wang, Z.; Zhao, G. Upscaling remote sensing inversion and dynamic monitoring of soil salinization in the Yellow River Delta, China. *Ecol. Indic.* **2023**, *148*, 110087. [CrossRef]

17. Hu, S.; Meng, K.; Ma, R.; Sun, Z.; Wang, Z.; Ge, M.; Zeng, L.; Yin, L. The potential risk of soil salinization on vegetation restoration by ecological water conveyance project in Qingtu Lake Wetland, northwestern China. *Land Degrad. Dev.* **2024**, *35*, 1296–1307. [CrossRef]

18. Sun, C.; Liu, Y.X.; Li, M.C.; Zhao, S.S.; Zhou, M.X. Spatiotemporal evolution of salt marsh and influential analysis of reclamation of Jiangsu middle coast in recent 25 years. *J. Nat. Resour.* **2015**, *30*, 1486–1498. [CrossRef]

19. Chen, F.; Hu, H.; Pan, D.; Wang, J.; Zhang, H.; Pan, Z. Distribution characteristics of rainfall erosivity in Jiangsu coastal areas. *Agronomy* **2023**, *13*, 1829. [CrossRef]

20. Zhang, Y.; Xiao, X.; Sun, Z.; Lei, B.; Li, M.; Guo, X.; Xing, C. Salt dynamic changes between seawater and phreatic brine in muddy tidal flats under tidal influence. *J. Hydrol.* **2024**, *634*, 131044. [CrossRef]

21. Jia, Y.; Wu, J.; Cheng, M.; Xia, X. Global Transfer of Salinization on Irrigated Land: Complex Network and Endogenous Structure. *SSRN Electron. J.* **2022**, *336*, 117592. [CrossRef]

22. Yang, N.; Cui, W.X.; Zhang, Z.T.; Zhang, J.R.; Chen, J.; Du, R.; Zhou, Y. Soil salinity inversion at different depths using improved spectral index with UAV multispectral remote sensing. *Trans. Chin. Soc. Agric. Eng.* **2020**, *36*, 13–21. [CrossRef]

23. Brady, N.C.; Weil, R.R. *The Nature and Properties of Soils*; Prentice Hall: Upper Saddle River, NJ, USA, 2008.

24. Blum, F.M.S.; Möhlhenrich, S.C.; Raith, S.; Pankert, T.; Peters, F.; Wolf, M.; Modabber, A. Clinical Oral Investigations. Evaluation of an artificial intelligence-based algorithm for automated localization of craniofacial landmarks. *Clin. Oral Investig.* **2023**, *27*, 2255–2265. [CrossRef] [PubMed]

25. Ahmad, S.; Kalra, A.; Stephen, H. Estimating soil moisture using remote sensing data: A machine learning approach. *Adv. Water Resour.* **2010**, *33*, 69–80. [CrossRef]

26. Pham, T.D.; Yokoya, N.; Nguyen, T.T.T.; Le, N.N.; Ha, N.T.; Xia, J.; Pham, T.D. Improvement of mangrove soil carbon stocks estimation in North Vietnam using Sentinel-2 data and machine learning approach. *GISci. Remote Sens.* **2021**, *58*, 68–87. [CrossRef]

27. Yang, W.; Hu, Y.; Hu, C.; Yang, M. An agent-based simulation of deep foundation pit emergency evacuation modeling in the presence of collapse disaster. *Symmetry* **2018**, *10*, 581. [CrossRef]

28. Mirjalili, S.; Lewis, A. The whale optimization algorithm. *Adv. Eng. Softw.* **2016**, *95*, 51–67. [CrossRef]

29. Allbed, A.; Kumar, L.; Aldakheel, Y.Y. Assessing soil salinity using soil salinity and vegetation indices derived from IKONOS high-spatial resolution imageries: Applications in a date palm dominated region. *Geoderma* **2014**, *230–231*, 1–8. [CrossRef]

30. Khan, N.M.; Rastoskuev, V.V.; Sato, Y.; Shiozawa, S. Assessment of hydrosaline land degradation by using a simple approach of remote sensing indicators. *Agric. Water Manag.* **2005**, *77*, 96–109. [CrossRef]

31. Douaoui, A.E.K.; Nicolas, H.; Walter, C. Detecting salinity hazards within a semiarid context by means of combining soil and remote-sensing data. *Geoderma* **2006**, *134*, 217–230. [CrossRef]

32. Abbas, A.; Khan, S. Using remote sensing techniques for appraisal of irrigated soil salinity. In Proceedings of the International Congress on Modelling and Simulation (MODSIM), Christchurch, New Zealand, 10–13 December 2007; Modelling and Simulation Society of Australia and New Zealand Inc.: Canberra, Australia, 2007; pp. 2632–2638.

33. Voitik, A.; Kravchenko, V.; Pushka, O.; Kutkovetska, T.; Shchur, T.; Kocira, S. Comparison of NDVI, NDRE, MSAVI and NDSI indices for early diagnosis of crop problems. *Agric. Eng.* **2023**, *27*, 47–57. [CrossRef]

34. Sirpa-Poma, J.W.; Satgé, F.; Pillco Zolá, R.; Resongles, E.; Perez-Flores, M.; Flores Colque, M.G.; Bonnet, M.P. Complementarity of Sentinel-1 and Sentinel-2 data for soil salinity monitoring to support sustainable agriculture practices in the Central Bolivian Altiplano. *Sustainability* **2024**, *16*, 6200. [CrossRef]

35. Mehla, M.K.; Kumar, A.; Kumar, S.; Jhorar, R.K. Soil salinity assessment and mapping using spectral indices and geostatistical techniques-concepts and review. In *Remote Sensing of Soils*; Elsevier: Amsterdam, The Netherlands, 2024; pp. 429–437.

36. Al-Kasoob, G.F.; Al-Sulttani, A.H.; Al-Quraishi, A.M.F.; Hussein, R.N. Monitoring drifting sand using spectral index and Landsat TM/OLI datasets in Bahr An-Najaf area, Iraq. In *Natural Resources Deterioration in MENA Region: Land Degradation, Soil Erosion, and Desertification*; Springer International Publishing: Cham, Switzerland, 2024; pp. 241–260. [CrossRef]

37. Zhang, Y.; Li, S.; Wang, L. Development of new spectral indices for soil salinity estimation using Landsat and Sentinel-2 data. *Environ. Monit. Assess.* **2023**, *195*, 579.

38. Ge, X.Y.; Ding, J.L.; Teng, D.X.; Wang, J.Z.; Huo, T.C.; Jin, X.Y.; Wang, J.J.; He, B.Z.; Han, L.J. Updated soil salinity with fine spatial resolution and high accuracy: The synergy of Sentinel-2 MSI, environmental covariates and hybrid machine learning approaches. *Catena* **2022**, *212*, 106054. [CrossRef]

39. Nosetto, M.D.; Acosta, A.M.; Jayawickreme, D.H.; Ballesteros, S.I.; Jackson, R.B.; Jobbágy, E.G. Land-use, and topography shape soil and groundwater salinity in central Argentina. *Agric. Water Manag.* **2013**, *129*, 120–129. [CrossRef]

40. Boudibi, S.; Sakaa, B.; Benguega, Z.; Fadlaoui, H.; Othman, T.; Bouzidi, N. Spatial prediction and modeling of soil salinity using simple cokriging, artificial neural networks, and support vector machines in El Outaya plain, Biskra, southeastern Algeria. *Acta Geochim.* **2021**, *40*, 390–408. [CrossRef]

41. Zhong, W.; Zhang, D.; Sun, Y.; Wang, Q. A CatBoost-Based Model for the Intensity Detection of Tropical Cyclones over the Western North Pacific Based on Satellite Cloud Images. *Remote Sens.* **2023**, *15*, 3510. [CrossRef]

42. NGatdula, N.; Blanco, A. Assessment of the vulnerability of coastal agriculture to seawater intrusion using remote sensing, GIS, and Multi-Criteria Decision Analysis. *Int. J. Digit. Earth* **2024**, *17*, 2367733. [CrossRef]

43. Khudhair, D.S. Evaluating Soil Texture and Elemental Composition in Wasit Governorate, Iraq: A Remote Sensing Approach. *J. Al-Muthanna Agric. Sci.* **2024**, *11*, 1–14. [CrossRef]

44. Zhang, J.; Zhang, Z.; Chen, J.; Chen, H.; Jin, J.; Han, J.; Wei, G. Estimating soil salinity with different fractional vegetation cover using remote sensing. *Land Degrad. Dev.* **2021**, *32*, 597–612. [CrossRef]